Engineering Experiment Station
of the Georgia Institute of Technology
Atlanta, Georgia

WIND-TUNNEL TEST RESULTS ON A SMALL SCALE-MODEL HELICOPTER ROTOR OVER THE USEFUL RANGE OF POSITIVE ROTOR ANGLES OF ATTACK AND A COMPARISON WITH THEORY

By

Walter Castles, Jr.

Daniel Guggenheim School of Aeronautics

o - o - o - o - o - o - o - o - o - o - o

Contract No. NAw-6512

National Aeronautics and Space Administration

April, 1959

WIND-TUNNEL TEST RESULTS ON A SMALL SCALE-MODEL HELICOPTER ROTOR OVER THE USEFUL RANGE OF POSITIVE ROTOR ANGLES OF ATTACK AND A COMPARISON WITH THEORY

By

Walter Castles, Jr.

Prepared by: [redacted]

Walter Castles, Jr., Professor
Daniel Guggenheim School of
Aeronautics

Approved by: [redacted]

Thomas W. Jackson, Chief
Mechanical Sciences Division

Released by: [redacted]

James E. Boyd, Director
Engineering Experiment Station

SUMMARY

Open-jet wind-tunnel tests were made on a two-bladed model helicopter rotor having a diameter of 4 feet and a solidity of 0.05 . The tests were run at $C_T = 0.004$ and covered the useful range of positive rotor angles of attack and helicopter flight path velocities. Measurements were made of the rotor thrust, torque, rpm, angle of attack of the plane of zero feathering, collective pitch, and first harmonic flapping.

A comparison of the test results with contemporary theory indicates two general ranges where discrepancies between calculated and measured values are large. The first is a low-speed range at large positive angles of attack covering values of $V/\Omega R$ from 0.02 to 0.10 and rotor angles of attack from 45° to 90° for the test value of $C_T = 0.004$. The second is a high-speed, low angle of attack range for which $V/\Omega R > 0.25$.

For the lower-speed flight conditions a series of photographs were taken of a tuft grid located on the longitudinal center-line plane of the rotor. The photographs, reproduced in sketch form, give some indication of the flow patterns for low-speed inclined descent and vertical descent.

INTRODUCTION

The survey test program described in this report was undertaken in an attempt to determine the positive angle of attack flight ranges wherein existing helicopter induced flow and blade element theory is adequate or else in need of improvement.

Since contemporary induced flow theory assumes that the wake vortex system consists of a uniform, semi-infinite, elliptic vortex cylinder, its accuracy appears questionable for partial-power, inclined descent flight conditions in which the wake may be of abnormal type. It also appears that present induced velocity theory may considerably underestimate the mean induced velocities at the blade axes for high-speed flight conditions in which the longitudinal spacing of the blade tip vortices in the wake becomes large.

NOTATION

A_0 mean blade pitch angle; also collective pitch

a_1 longitudinal blade flapping angle measured with respect to the plane of zero feathering; also lateral cyclic pitch coefficient measured with respect to the tip-path plane

b number of blades in a rotor

b_1 lateral blade flapping angle measured with respect to the plane of zero feathering; also longitudinal cyclic pitch coefficient measured with respect to the tip-path plane

C_Q rotor torque coefficient ($Q/\rho\pi\Omega^2R^5$)

ΔC_Q increment in rotor torque coefficient above that for zero thrust and zero freestream velocity

C_T rotor thrust coefficient ($T/\rho\pi\Omega^2R^4$)

c blade chord at radius r

$\bar{c}$ mean blade chord defined by

$$\bar{c} = \int_0^R cr^2dr \Big/ \int_0^R r^2dr$$

c_{d_o} section profile-drag coefficient

Δc_{d_o} increment in section profile-drag coefficient above that for zero section lift coefficient

c_ℓ section lift coefficient

P_i induced power

Q rotor torque

R rotor radius

R_e effective rotor radius ($R - \frac{1}{2}$ blade tip chord)

r radial distance of a blade element from the rotor hub

T rotor thrust

V freestream velocity

v mean normal component of induced velocity over the rotor disk

v_o the quantity $(T/2\rho\pi R^2)^{1/2}$

α angle of attack of plane of zero feathering

α_v angle of attack of tip-path plane $(\alpha + a_1)$

λ_v inflow velocity ratio at center of tip-path plane given by

$$\lambda_v = (V\sin\alpha_v - v)/\Omega R$$

λ_z nondimensional normal component of flight path velocity given by

$$\lambda_z = V\sin\alpha_v/(\Omega R\sqrt{\tfrac{1}{2} C_T})$$

μ_v nondimensional in-plane component of flight path velocity given by

$$\mu_v = V\cos\alpha_v/\Omega R$$

ρ air density

σ rotor solidity $(b\bar{c}/\pi R)$

ψ azimuth angle measured in direction of rotor rotation from downwind axis of rotor plane

Ω rotor angular velocity

APPARATUS

Wind-Tunnel

The open-jet wind-tunnel configuration used for the present tests was the same as that described in reference 1 except for the addition of a ground plane (side-wall) which spanned the side of the open-jet. It was located at a distance from the tunnel and rotor center-lines such that the open-jet wind-tunnel wall correction was essentially zero for a lifting line coinciding with the lateral diameter of the rotor.

Rotor Test Stand

The rotor test stand was the same as that described in reference 1 except for the following modifications:

1. The drive system was altered to permit use of the wind-tunnel balance yaw mechanism for setting and measuring the angle of attack of the rotor plane of zero feathering (i.e., model shaft axes) .

2. The hub assembly was modified to accomodate the teetering model rotor.

3. Three micrometer type electric feeler contacts were installed on the outside of the housing at $\psi = 0^\circ$, 90°, and 270° in order to measure the rotor flapping angles.

The above-mentioned electric feelers made contact with machined surfaces on the blade roots in such a way as to indicate contact by neon glow-lamp indicators. The extension of the feelers to the contact surfaces was actuated and measured by autosyns coupled to counters. The feelers were kept in retracted position except for the momentary extensions

to contact position when flapping angle measurements were being made.

Model Rotor

The model rotor was a two-bladed, teetering type with over 20° of flapping freedom and solidity $\sigma = 0.05$. The blades had a 2/1 taper ratio, which was used to obtain adequate blade strength for the rough flow conditions in low-speed, power-on descent, and an NACA 43015 airfoil section. This airfoil section was used in order to obtain more nearly full-scale maximum lift coefficients than could be obtained from the usual rotor airfoils at the low test Reynolds numbers. The blades were constructed with steel leading edges and laminated walnut trailing edges similar to the tapered blades shown in reference 1. The hub blade sockets were built with zero initial cone angle, and the blades were sufficiently stiff so that there was no measurable coning angle during the tests. The model rotor assembly is shown in figure 1.

Tuft Grid

The tuft grid was located in the longitudinal rotor center-plane and rotated with the plane of zero feathering. The tufts were spaced on 6 inch centers and covered a circular area having a radius of approximately 4 feet about the rotor hub. Figure 2 is a photograph of the test set-up in operation.

TEST PROCEDURE

The freestream velocity (i.e., wind-tunnel fan rpm), rotor rpm, and rotor thrust were held constant for each test run, and measurements were made of the rotor torque, collective pitch angle, and longitudinal and lateral components of the flapping angle for a series of settings of the angle of attack of the plane of zero feathering covering a range from -5° up to an angle which yielded a negative torque coefficient.

The operating procedure was essentially the same as that reported in reference 1 except for the additional measurements of flapping angles and rotor angles of attack.

REDUCTION OF DATA

The reference collective pitch angle, A_0 , was obtained from the test data by reducing each value measured at the blade root by the calculated dynamic twist at the three-quarter radius point. This correction amounted to 2.5 per cent for the 1200 rpm operating condition.

The measured torque at zero thrust and zero forward speed was subtracted out on each run in order to eliminate the rather large tare torque and also to compensate for the relatively unknown portion of the rotor torque attributable to the constant term in the mathematical approximation which relates the blade element profile-drag coefficient and the blade element lift coefficient. In view of the low blade airfoil Reynolds numbers of these tests, eliminating the tare torque appeared to be more important than trying to deduce an accurate value for the minimum blade profile-drag.

No corrections were made in the measured values of the longitudinal and lateral flapping coefficients.

THEORETICAL CALCULATIONS

For the forward flight runs, theoretical values for the collective pitch angle, A_0, and the flapping coefficients, a_1 and b_1, were computed by means of equations 72, 73, and 75 of reference 2, using an effective blade radius, R_e, equal to the actual blade radius, R, minus half the tip chord. In these calculations the thrust, rotor angle of attack, freestream velocity, and rotational velocity were taken as the known quantities.

Theoretical values of the incremental increase in rotor torque coefficient, ΔC_Q, over that calculated for the zero thrust and zero freestream velocity condition were computed from equation 90b of reference 2. These calculations were made under the assumption that the variation of blade element profile-drag coefficient with section lift coefficient had the form

$$\Delta c_{d_o} = 0.02\, c_\ell^{\,2} \qquad (1)$$

No correction was made for blade stall or reverse flow effects.

Theoretical values of the collective pitch, A_0, and incremental rotor torque coefficient, ΔC_Q, for vertical descent conditions were computed from the theoretical values of induced power required for a rotor with triangular disk loading, given in reference 3. The procedure was to calculate an equivalent uniform induced velocity ratio

$$\frac{v}{\Omega R} = \frac{P_i}{T v_o}\sqrt{\frac{1}{2} C_T} \qquad (2)$$

for use in the equations of reference 2.

COMPARISON OF THEORETICAL AND EXPERIMENTAL RESULTS

In figures 3a through 3j plots of the measured and calculated values of the collective pitch angle, A_0, versus the angle of attack, α_v, of the tip-path plane are compared for various test values of the forward to tip-speed ratio, $V/\Omega R$. In the low-speed runs, for which the rotor torque remained positive (i.e., $V/\Omega R \leqq 0.1$), α_v covers the full range from 0° to 90°. For the higher-speed runs, the range of α_v was terminated at the value for which the torque became negative.

Plots of the measured and calculated values of a_1 versus α_v are compared in figures 4a through 4j for various values of $V/\Omega R$. These plots show values of the longitudinal flapping angle, a_1, measured with respect to the plane of zero feathering, or the equivalent values of the lateral cyclic pitch coefficient, also a_1, measured with respect to the tip-path plane.

Similarly, figures 5a through 5h show a comparison of the measured and calculated values of the lateral flapping angle, b_1, measured with respect to the plane of zero feathering, or the equivalent longitudinal cyclic pitch coefficient measured with respect to the tip-path plane.

In figures 6a through 6j experimental and calculated values of the increment, ΔC_Q, in rotor torque coefficient are plotted versus α_v. In these plots, ΔC_Q represents the increase in rotor torque coefficient C_Q for the test conditions over that for the zero freestream velocity and

zero thrust condition.

Plots of measured and calculated values of the collective pitch, A_0 , and torque coefficient increment, ΔC_Q , versus $V/\Omega R$ for the vertical descent runs are shown in figures 7a through 7d . The calculated values are shown both with and without a correction for effective radius, R_e .

TUFT STUDY RESULTS

Line tracings were made of the tuft pattern photographs for purposes of reproduction. These are shown in figures 8 and 9 .

Figures 8a through 8j show the tuft patterns in a central cross section of the flow for various equilibrium rates of vertical descent between hovering and a point well into the windmill state.

Figures 9a through 9e show the tuft patterns for each positive 15° increment in rotor angle of attack of plane of zero feathering between hovering and vertical descent ($V/\Omega R \approx 0.075$) .

The tuft photographs taken at higher freestream velocity ratios (i.e., $0.1 \leq V/\Omega R \leq 0.4$) did not show any definite regions of recirculation or large, abrupt change of flow direction. Consequently, they were not reproduced.

DISCUSSION

Figures 3 and 6, which compare theoretical and experimental values of the collective pitch, A_0, and the incremental torque coefficient, ΔC_Q, respectively, can be used to estimate the errors in the theoretical values of the mean induced velocity, v, for the lower-speed flight conditions where there is no significant blade stall. For example, if the measured values of A_0 and ΔC_Q decrease more rapidly than their theoretical values as the flight path velocity, V, increases at some constant rotor angle of attack, α_v, it indicates that the mean induced velocity, v, at each test condition, also decreases more rapidly with increasing V than does its theoretical value as calculated from equation 2 of reference 1, namely

$$\frac{v}{\Omega R} = \frac{C_T/2}{(1 - \frac{3}{2}\mu_v^2)\sqrt{\lambda_v^2 + \mu_v^2}} \qquad (3)$$

wherein λ_v is the inflow velocity ratio at the center of the tip-path plane given by

$$\lambda_v = \frac{V\sin\alpha_v - v}{\Omega R} \qquad (4)$$

Figures 3a and 6a indicate that for the very low-speed

flight conditions ($V/\Omega R \gtrsim 0.02$) the calculated and measured values of the collective pitch and incremental torque coefficient are in good agreement. At low positive rotor angles of attack this initial agreement persists up to flight velocity ratios of about $V/\Omega R = 0.2$ for the two-bladed rotor operating at $C_T = 0.004$ as indicated by figures 3b through 3f and figures 6b through 6f . However, from figures 3c and 6c it appears that the theory overestimates the induced velocities for the high angle of attack range ($50^\circ \leqq \alpha_v \leqq 90^\circ$) at speed ratios in the vicinity of $V/\Omega R = 0.08$ for the two-bladed rotor.

In the higher speed range of the tests ($0.2 < V/\Omega R < 0.43$) a progressive underestimation of the equilibrium values of A_0 and ΔC_Q with increasing V is indicated. Part of this discrepancy is undoubtedly due to stall effects on the retreating blade which were neglected in calculating the theoretical values. However, some of the error probably originates in an underestimation of the instantaneous induced velocity at the blade axes. For example, the calculated average value of the induced velocity at the blade axes as given in reference 4 for a two-bladed rotor operating at $V/\Omega R \gtrsim 0.4$ and small negative rotor angle of attack is 60 per cent higher than the usually assumed theoretical value obtained from equation 3 .

Figure 4 , which compares the calculated and measured values of the longitudinal blade flapping coefficient, a_1 , measured with respect to the plane of zero feathering (or lateral cyclic pitch coefficient measured with respect to the tip-path plane), indicates an overestimation of the equilibrium value by present theory in the low forward speed and intermediate positive angle of attack range.

The maximum deviation between theory and experiment appears to be at about $\alpha_v = 40^\circ$ for $V/\Omega R = 0.06$. It moves to about $\alpha_v = 15^\circ$ as the speed ratio increases to $V/\Omega R = 0.10$. The differences appear to decrease with further increase in speed until the speed ratio reaches $V/\Omega R = 0.22$. Above this speed ratio the theory (neglecting stall effects) appears to progressively underestimate the equilibrium value of a_1 by an amount which is greatest at the lowest rotor angle of attack. For example, at $V/\Omega R = 0.43$ and $\alpha_v = 7^\circ$ (figure 4j) the measured value of a_1 is about double the calculated value. Most of the disagreement between the high-speed theoretical and experimental values of a_1 probably arises from neglecting tip-stall effects in the elementary blade element theory, although a part of the difference may be due to an underestimation of the effective lateral induced velocity variation.

In the low-speed range, the discrepancies between the theoretical and experimental values of a_1 are probably introduced, at least in part, by the assumed uniform induced velocity in the theory. For example, if the distribution of induced velocity along the blade radii is assumed to be triangular rather than uniform, the calculated equilibrium values of a_1 are decreased for the low-speed flight conditions at positive rotor angles of attack. This is because of the inward shift in the blade loading.

Figure 5 indicates that the calculated and experimental values of the lateral blade flapping coefficient, b_1 , measured with respect to the plane of zero feathering (or the longitudinal cyclic pitch coefficient measured with respect to the tip-path plane), are in good

agreement except for those flight conditions encompassing the higher rotor angles of attack at speed ratios in the vicinity of $V/\Omega R = 0.08$. The tuft studies indicate abnormal flow patterns in this flight range.

Figure 7 shows a comparison of the measured values of A_0 and ΔC_Q for the two-bladed model rotor operating in vertical descent with those calculated from the approximate theory for a rotor having an infinite number of blades given in reference 3. Although the results obtained from the small-scale wind-tunnel test data can not be considered conclusive, it appears from the results of the present tests that a rotor with few blades may be more efficient under vertical descent flight conditions than one having a large number of blades. That is, the equilibrium values of the collective pitch and power required for a two-bladed rotor may be less than the values indicated by the theory of reference 3, which theory appears to be in reasonable agreement with the results of similar tests on three-bladed model rotors.

Figure 8, which shows a set of tuft patterns for a succession of steady-state vertical descent conditions, indicates that a hovering type wake persists to descent velocities of the order of 75 per cent of the hovering induced velocity. Thereafter, the extent of the columnar wake below the rotor shortens very rapidly with increasing equilibrium rate of descent and virtually disappears at a descent velocity about equal to the hovering induced velocity. At this rate of descent the center of the flow recirculation appears to lie in the rotor plane at about a half rotor radius outboard of the rotor disk. As the rate of descent is increased, the center of the flow recirculation appears to move upward and inward with respect to the rotor until, at the

power-off autorotation point, the center of the remaining weak recirculation is about a rotor radius above the rim of the rotor disk. It is the author's opinion that there may be considerable difference between the recirculatory type flow patterns for rotors having two and three or more blades, so that the present tuft studies probably should not be assumed valid for the latter type rotors.

Figure 9 shows a set of tuft patterns at 15° increments in positive rotor angle of attack of the plane of zero feathering for the speed ratio $V/\Omega R \simeq 0.075$ which corresponds to a flight path velocity about equal to that for power-off vertical descent or about $\sqrt{3}$ times hovering induced velocity. These patterns indicate that a region of recirculatory flow develops above and slightly behind the rotor at an angle of attack of the order of 30° and moves up and slightly forward as the rotor angle of attack is increased. The flow about the forward center region of the rotor disk appears to remain relatively free of large irregularities up to an angle of attack of about 75°. It should be noted that the present tuft studies indicate only the flow direction on the longitudinal center-plane of the rotor and furnish no indication of the type flow about the lateral sectors of the rotor disk.

Photographs taken of the tuft patterns for the higher speed range indicated no noticeable irregularities in the flow in the longitudinal center-plane for flight path velocities equal to or greater than twice the hovering induced velocity. In this range the flow appeared to be of potential type.

CONCLUSIONS

For the subject two-bladed, small-scale test rotor operated at $C_T = 0.004$ a comparison of the test results with contemporary theory indicates two general ranges of flight conditions where discrepancies between calculated and measured values of the blade angles and/or power required are large. The first is a low-speed, large positive rotor angle of attack region covering values of the speed ratio $0.02 < V/\Omega R < 0.10$ and angles of attack $45^\circ < \alpha_v < 90^\circ$. This low-speed flight range can probably be generalized for other values of C_T by expressing the flight path velocity ratio in terms of the hovering induced velocity ratio, $V/\sqrt{\frac{T}{2\rho\pi R^2}}$, in which case $V/\sqrt{\frac{T}{2\rho\pi R^2}}$ ranges from 0.2 to 2.0. From the limited amount of data made available by the present tests and similar data in reference 1, it appears that there may be some significant differences between the average induced velocities at the blade axes of two and three-bladed rotors operating in vertical (or steeply inclined) power-on descent. A large part of the discrepancy between the theoretical and experimental values of the rotor parameters for the low-speed, high angle of attack flight conditions is almost certainly attributable to errors in the theoretical estimation of the magnitude and distribution of the induced velocity at the blade axes.

The second range of flight conditions wherein large differences between the theoretical and measured values of the rotor parameters exist is the high-speed, low rotor angle of attack region for which

$V/\Omega R$ is greater than about 0.25 . In the cases of the collective pitch, longitudinal flapping angle, and incremental torque coefficient, a large part of the discrepancies are undoubtedly attributable to the neglect of blade stall effects in the equations used for obtaining the calculated values given in this report; however, a significant part of the error may arise from a gross underestimation by contemporary theory of the induced velocity at the blade axes of two-bladed rotors operating at large forward speed ratios. From an analysis of the present results it appears that the effective lateral induced velocity variation may be greater at the higher speed ratios than has been previously estimated.

For the two-bladed model rotor tested, the tuft studies indicated that a hovering type columnar wake existed below the rotor for power-on, equilibrium rates of vertical descent less than about 75 per cent of the mean hovering induced velocity. The tuft patterns also indicated that, in inclined descent, the flow in the longitudinal center-plane of the rotor disk was free of any large regions of recirculation or large-scale turbulence for flight path velocities greater than about twice the mean induced velocity in hovering.

REFERENCES

1. Castles, Walter Jr. and Gray, Robin B.: Empirical Relation between Induced Velocity, Thrust, and Rate of Descent of a Helicopter Rotor as Determined by Wind-Tunnel Tests on Four Model Rotors. NACA TN 2474, October 1951.

2. Castles, Walter Jr. and New, Noah C.: A Blade-Element Analysis for Lifting Rotors that is Applicable for Large Inflow and Blade Angles and Any Reasonable Blade Geometry. NACA TN 2656, July 1952.

3. Castles, Walter Jr.: Flow Induced by a Rotor in Power-On Vertical Descent. NACA TN 4330, July 1958.

4. Castles, Walter Jr. and Durham, Howard L. Jr.: The Computed Instantaneous Velocities Induced at the Blade Axes by the Skewed Helical Vortices in the Wake of a Lifting Rotor in Forward Flight. ASTIA Doc. No. AD-210 613, March 1959.

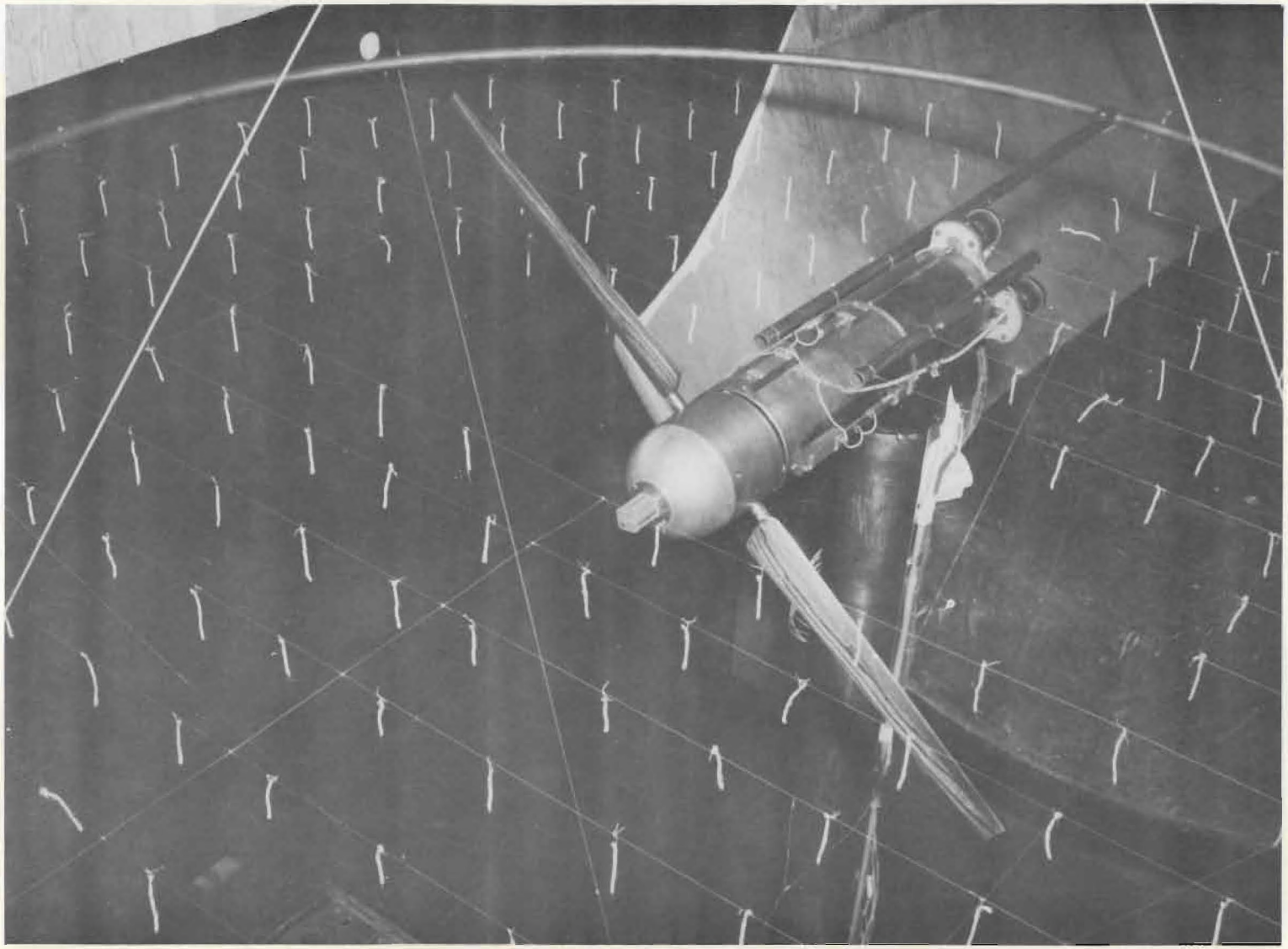

Figure 1. Model Rotor Assembly.

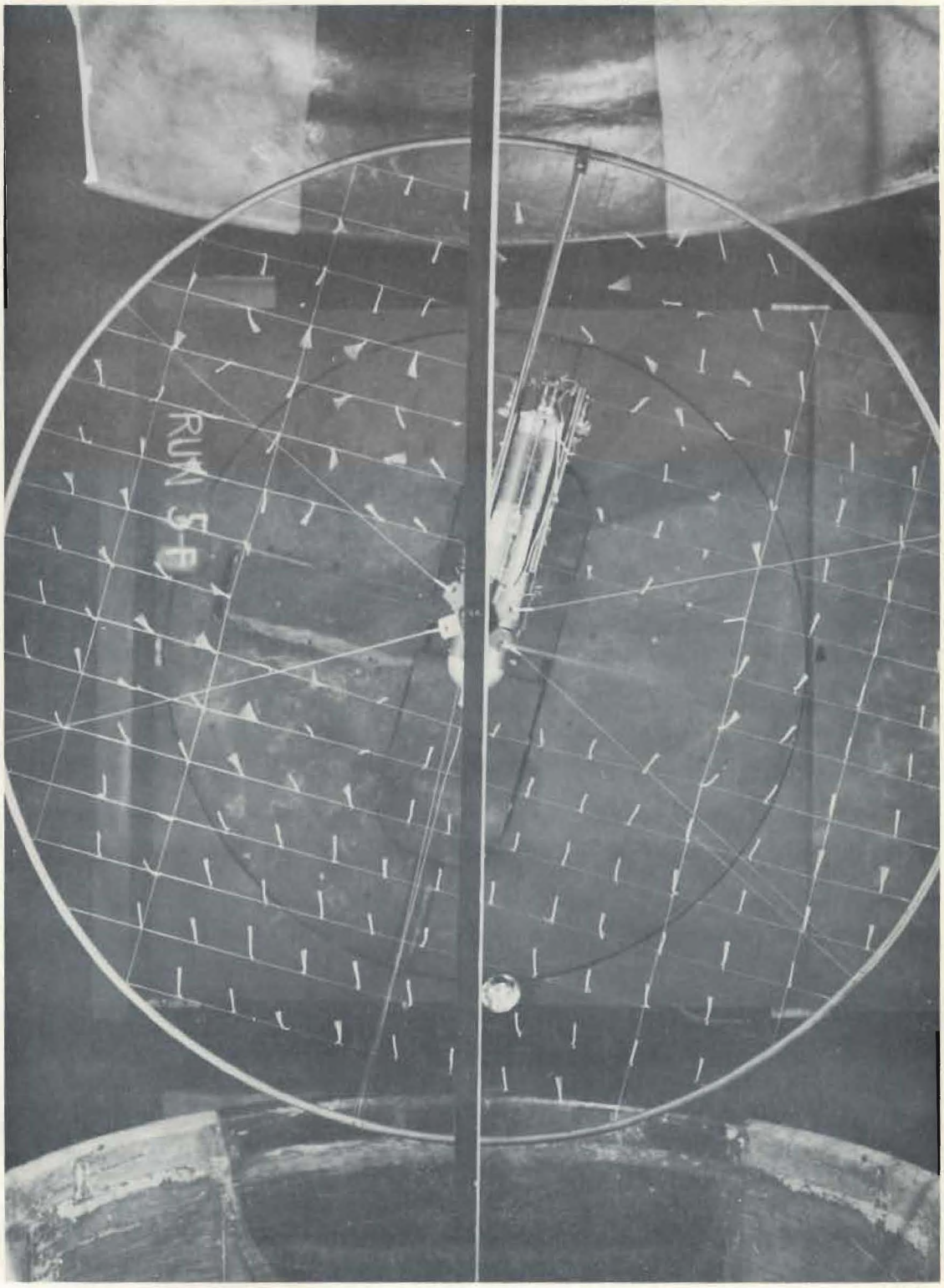

Figure 2. The Test Set-Up In Operation.

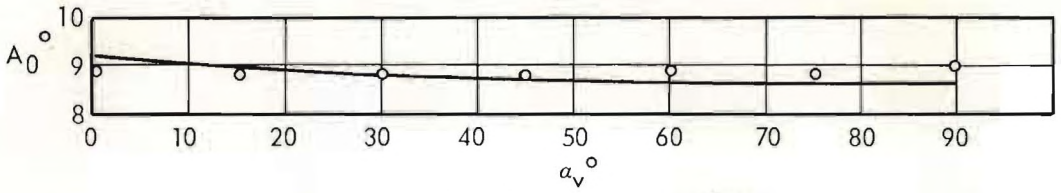

(a) V/ΩR = 0.02 (RPM = 1200)

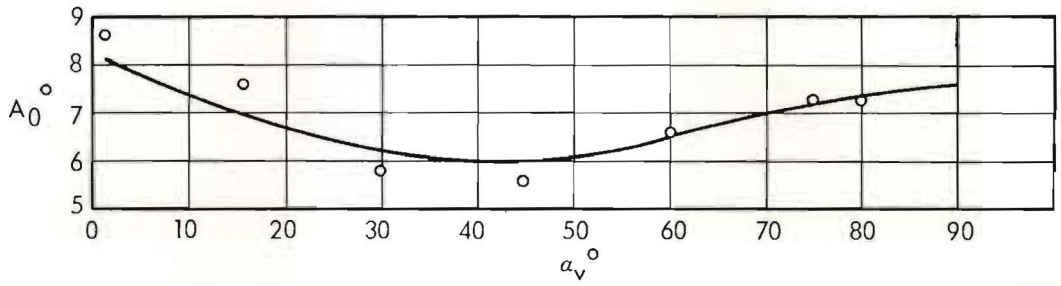

(b) V/ΩR = 0.06 (RPM = 1200)

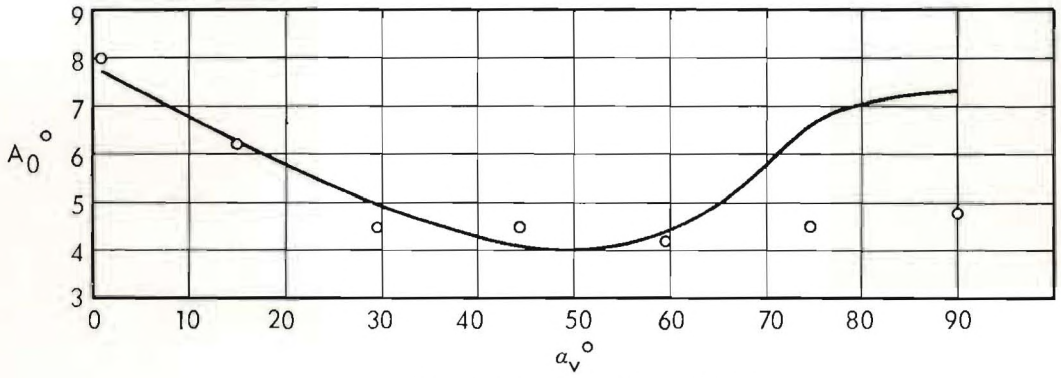

(c) V/ΩR = 0.08 (RPM = 1200)

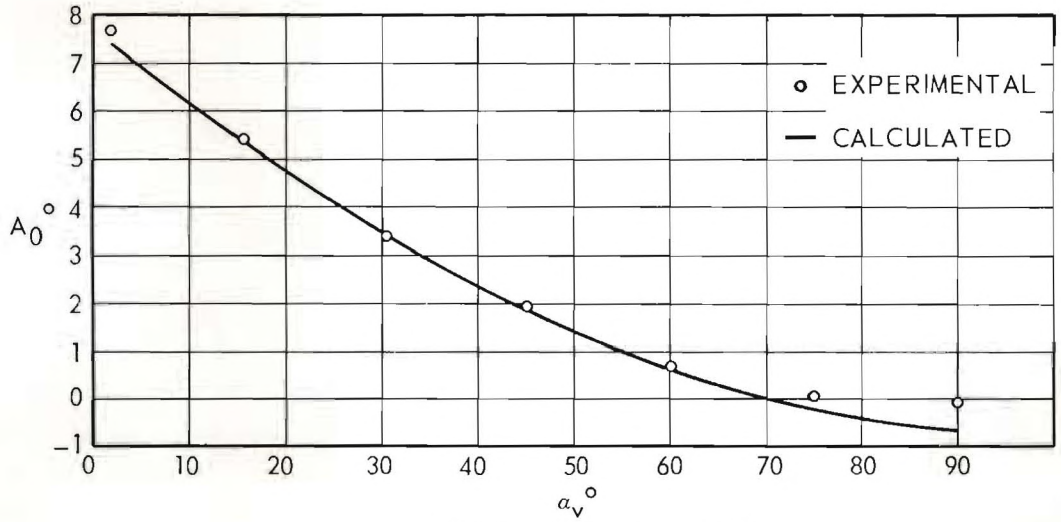

(d) V/ΩR = 0.10 (RPM = 1200)

Figure 3. Experimental and Calculated Values of A_0 versus a_v.

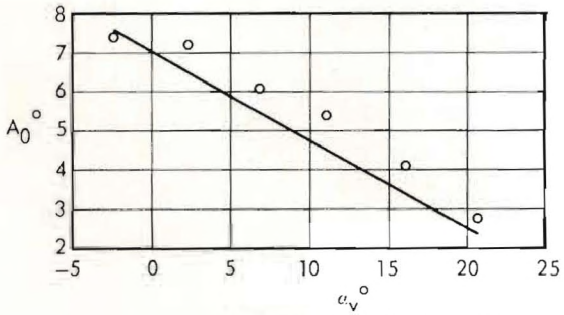

(e) V/ΩR = 0.14 (RPM = 1200)

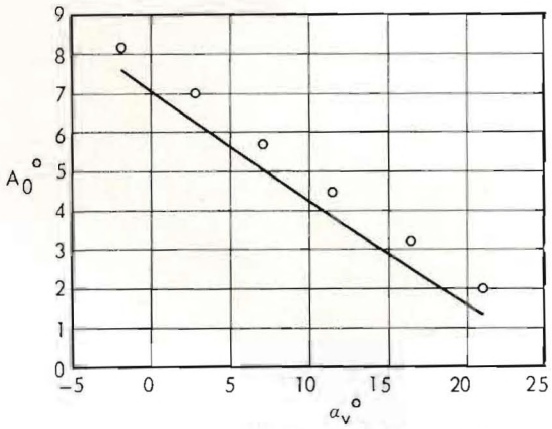

(f) V/ΩR = 0.18 (RPM = 1200)

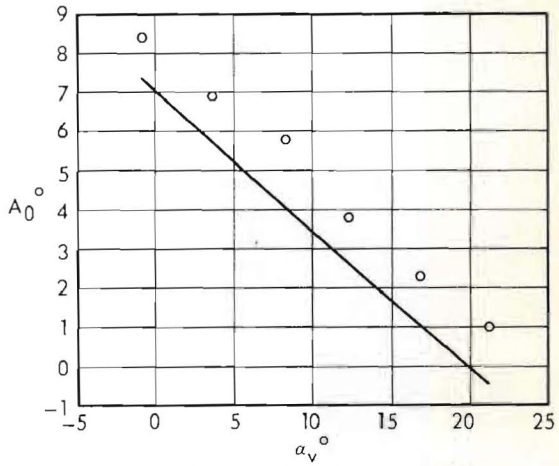

(g) V/ΩR = 0.22 (RPM = 1200)

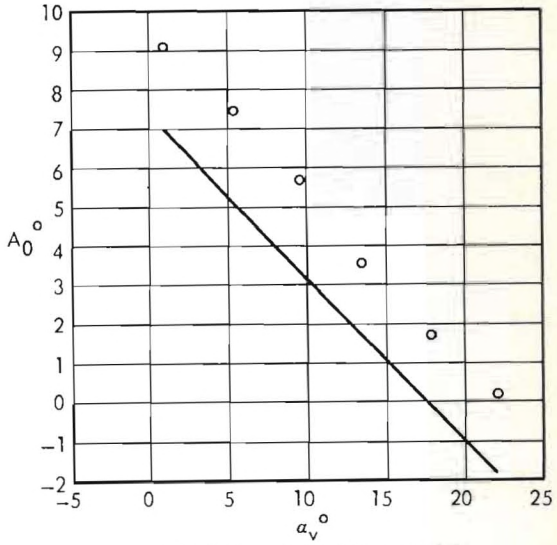

(h) V/ΩR = 0.26 (RPM = 1000)

Figure 3 (Continued).

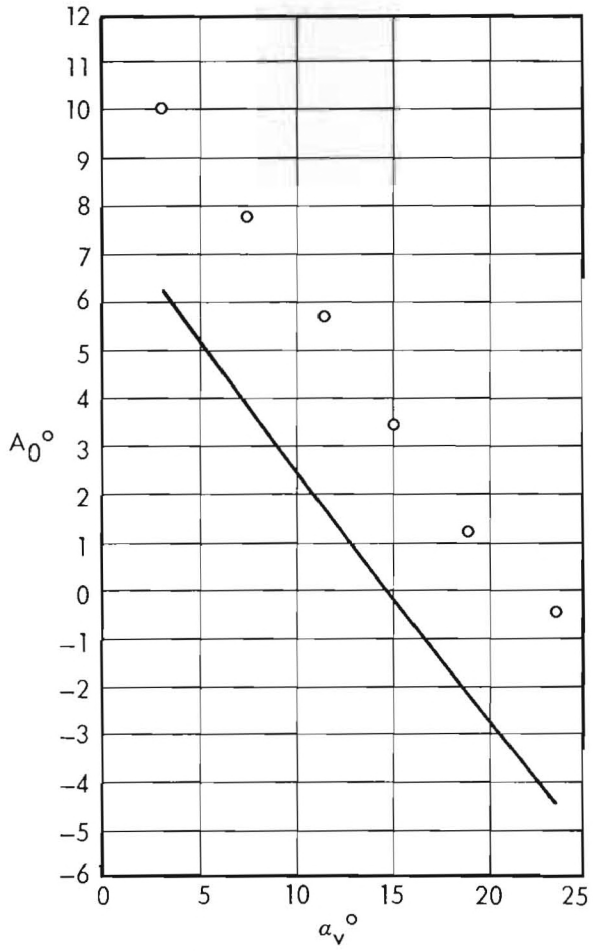

(i) V/ΩR = 0.32 (RPM = 800)

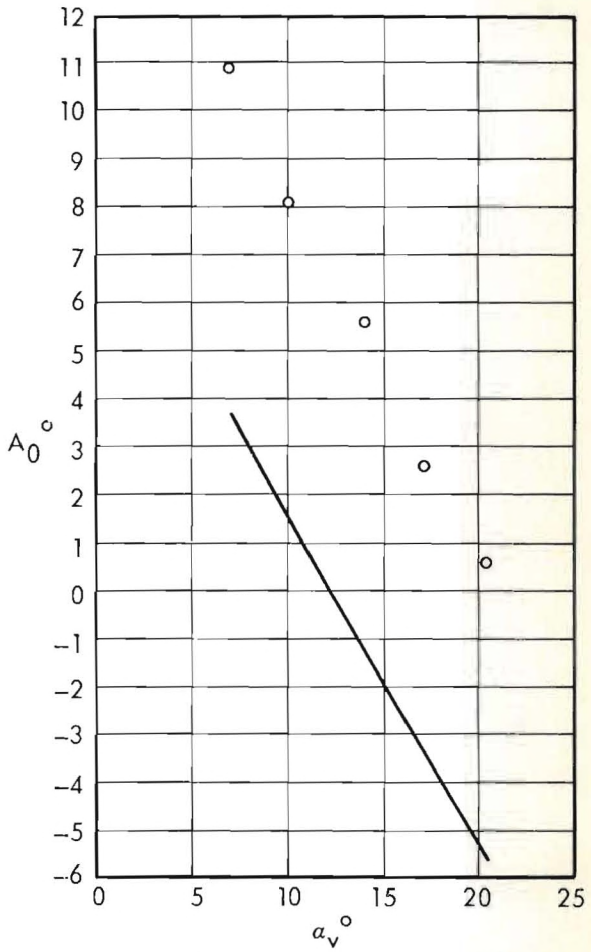

(j) V/ΩR = 0.43 (RPM = 600)

Figure 3 (Continued).

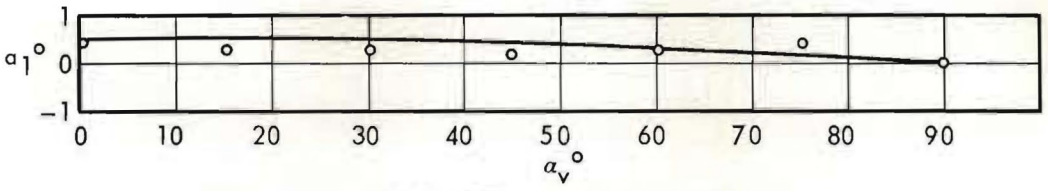

(a) V/ΩR = 0.02 (RPM = 1200)

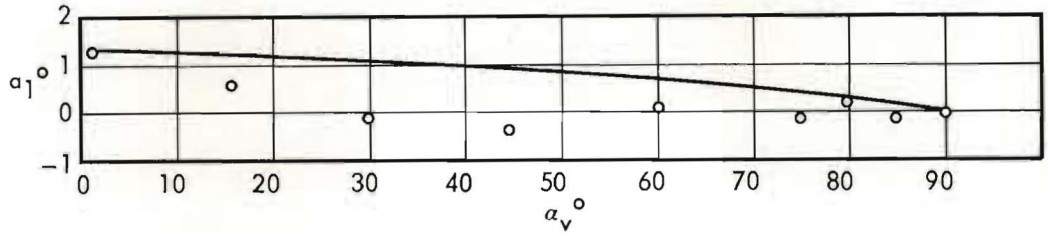

(b) V/ΩR = 0.06 (RPM = 1200)

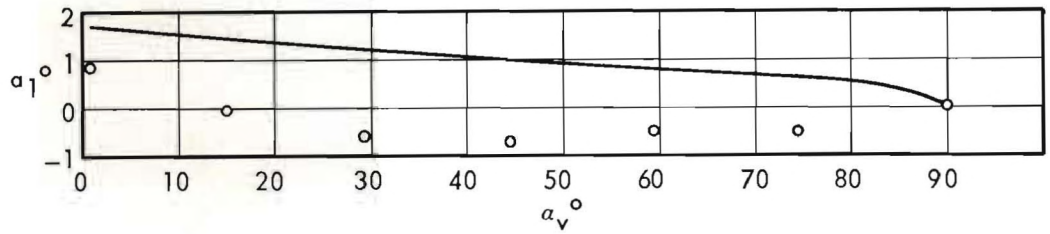

(c) V/ΩR = 0.08 (RPM = 1200)

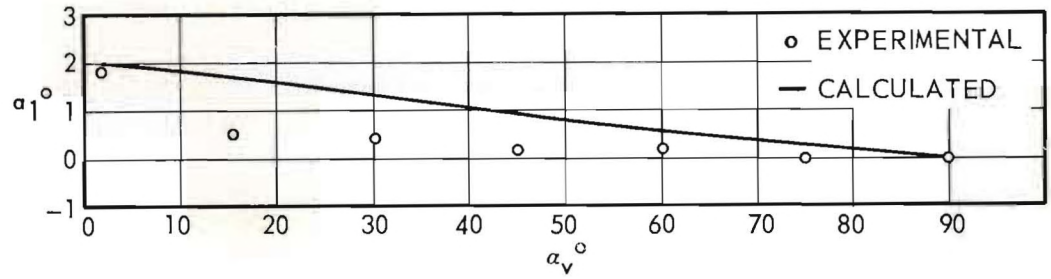

(d) V/ΩR = 0.10 (RPM = 1200)

Figure 4. Experimental and Calculated Values of a_1 versus α_v.

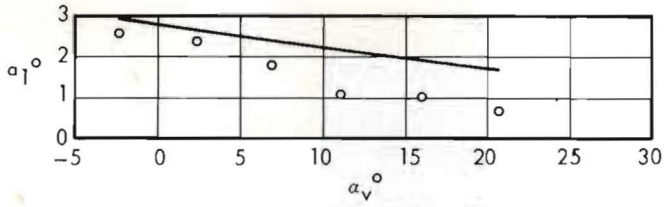

(e) V/ΩR = 0.14 (RPM = 1200)

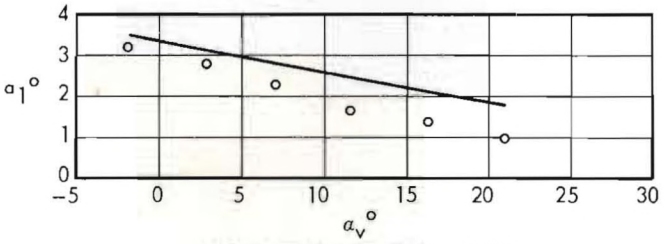

(f) V/ΩR = 0.18 (RPM = 1200)

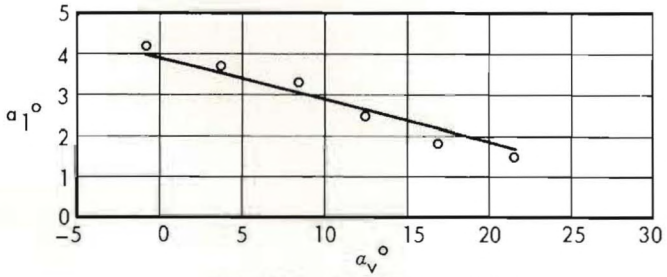

(g) V/ΩR = 0.22 (RPM = 1200)

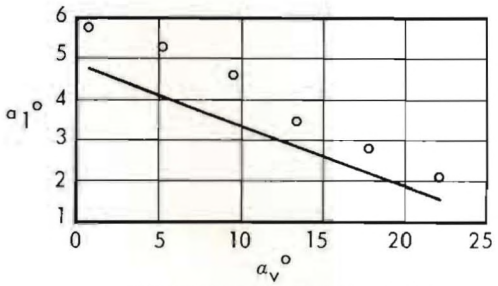

(h) V/ΩR = 0.26 (RPM = 1000)

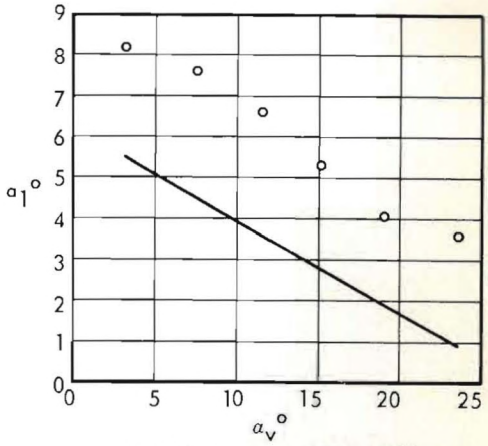

(i) V/ΩR = 0.32 (RPM = 800)

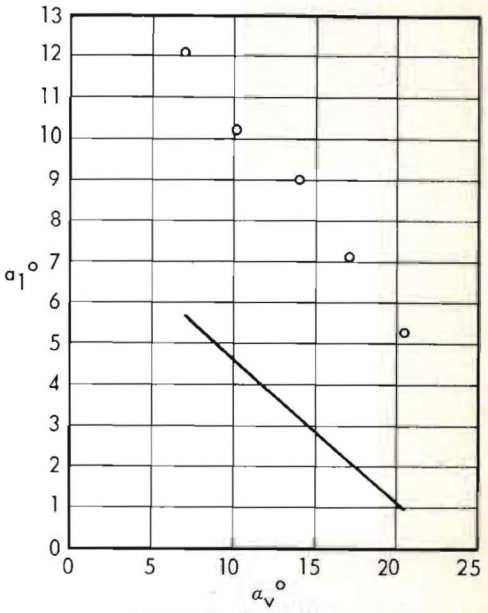

(j) V/ΩR = 0.43 (RPM = 600)

Figure 4 (Continued).

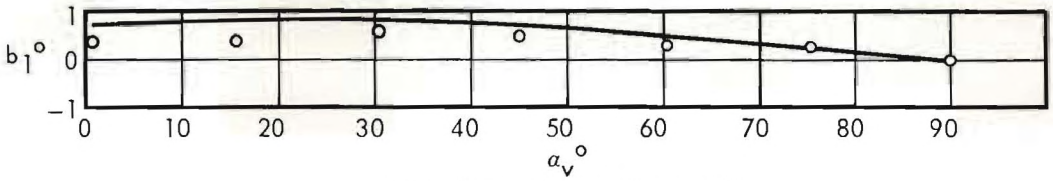

(a) V/ΩR = 0.02 (RPM = 1200)

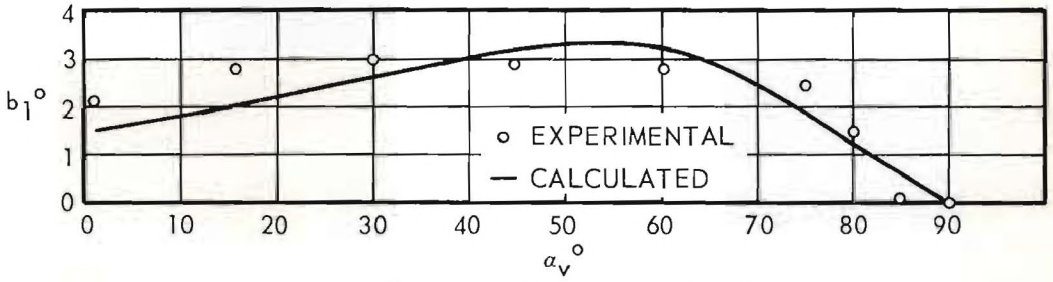

(b) V/ΩR = 0.06 (RPM = 1200)

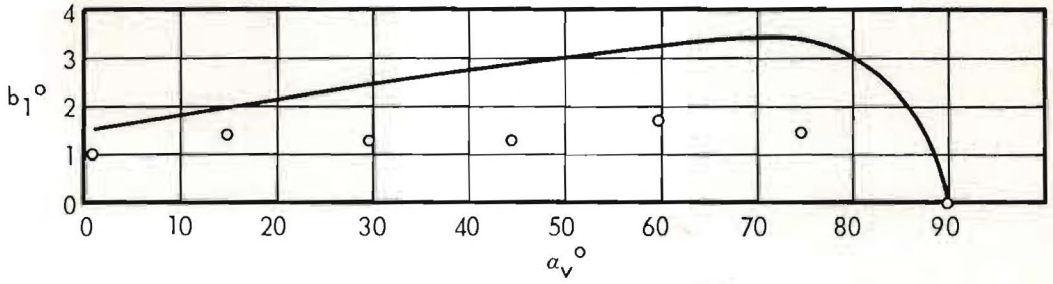

(c) V/ΩR = 0.08 (RPM = 1200)

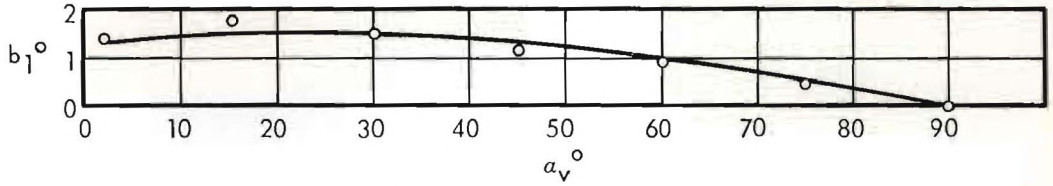

(d) V/ΩR = 0.10 (RPM = 1200)

Figure 5. Experimental and Calculated Values of b_1 versus a_v.

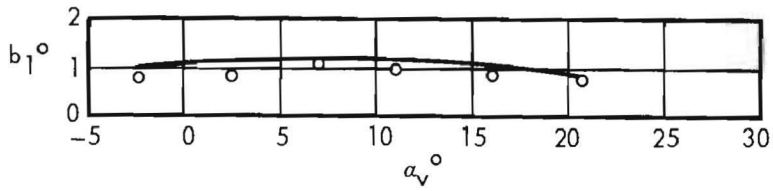

(e) V/ΩR = 0.14 (RPM = 1200)

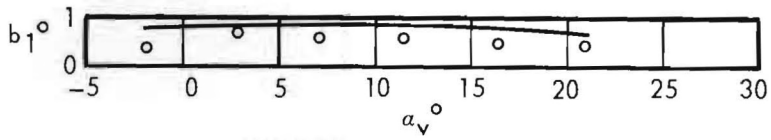

(f) V/ΩR = 0.18 (RPM = 1200)

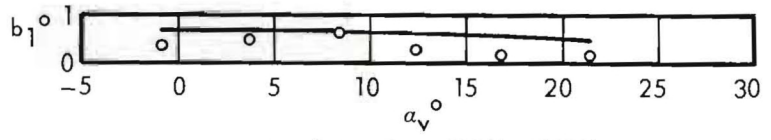

(g) V/ΩR = 0.22 (RPM = 1200)

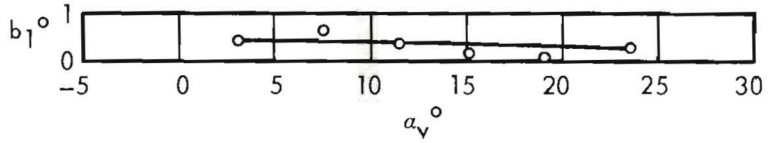

(h) V/ΩR = 0.32 (RPM = 800)

Figure 5 (Continued).

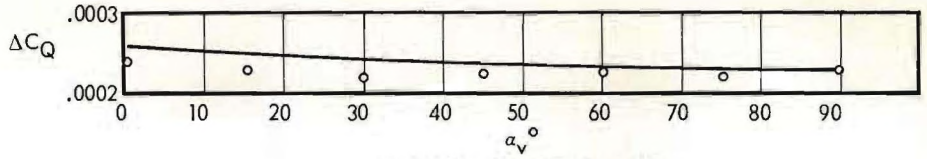

(a) V/ΩR = 0.02 (RPM = 1200)

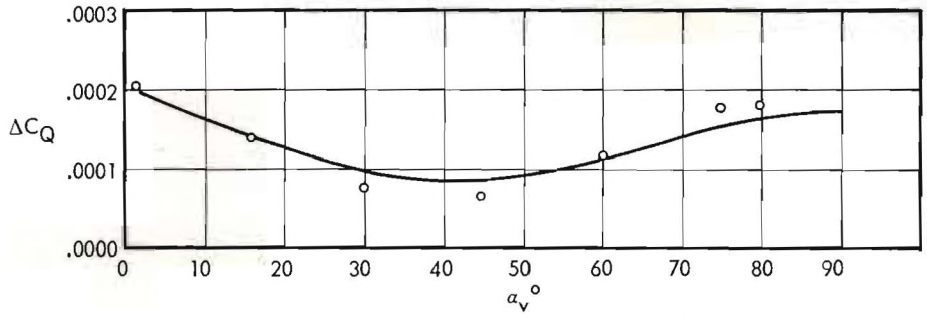

(b) V/ΩR = 0.06 (RPM = 1200)

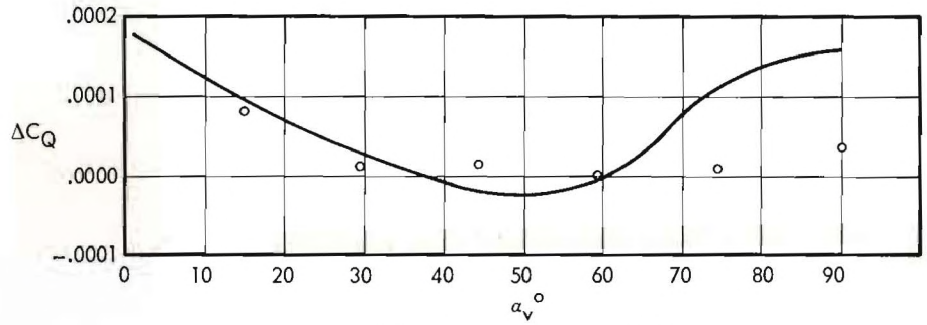

(c) V/ΩR = 0.08 (RPM = 1200)

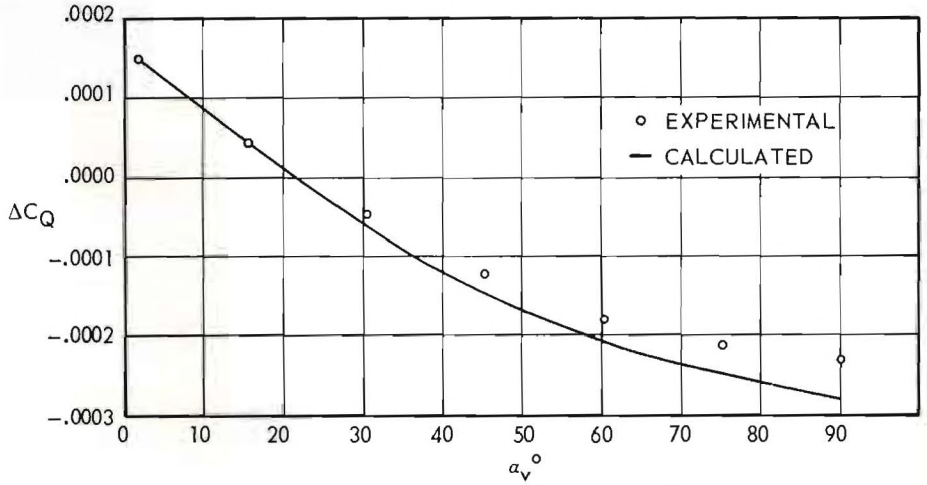

(d) V/ΩR = 0.10 (RPM = 1200)

Figure 6. Experimental and Calculated Values of ΔC_Q, the Increment of C_Q Above that for T = V = 0, versus α_V.

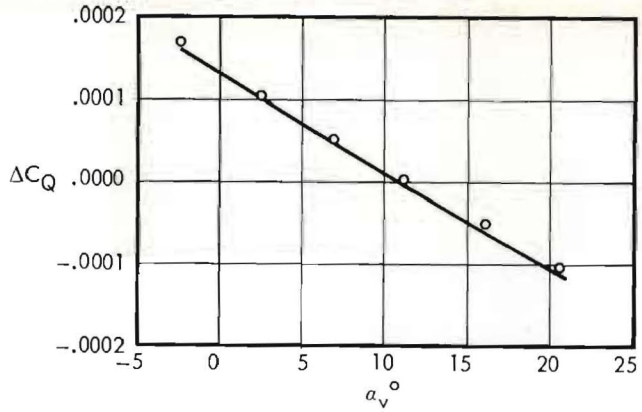

(e) V/ΩR = 0.14 (RPM = 1200)

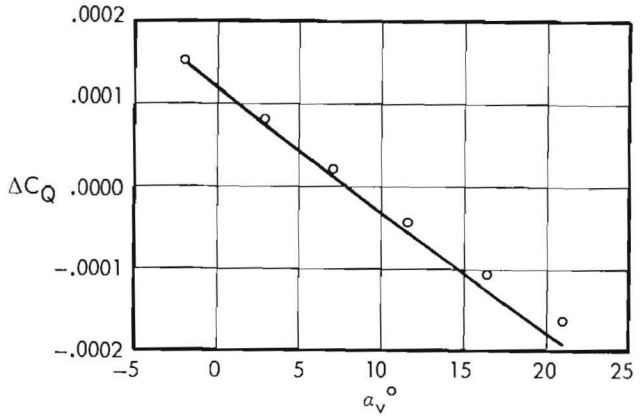

(f) V/ΩR = 0.18 (RPM = 1200)

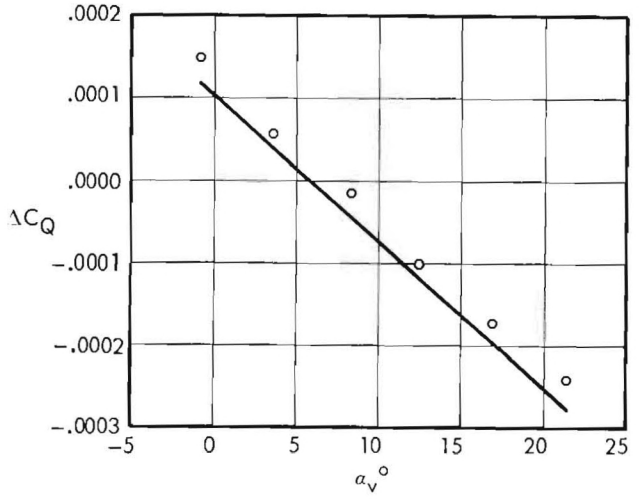

(g) V/ΩR = 0.22 (RPM = 1200)

Figure 6 (Continued).

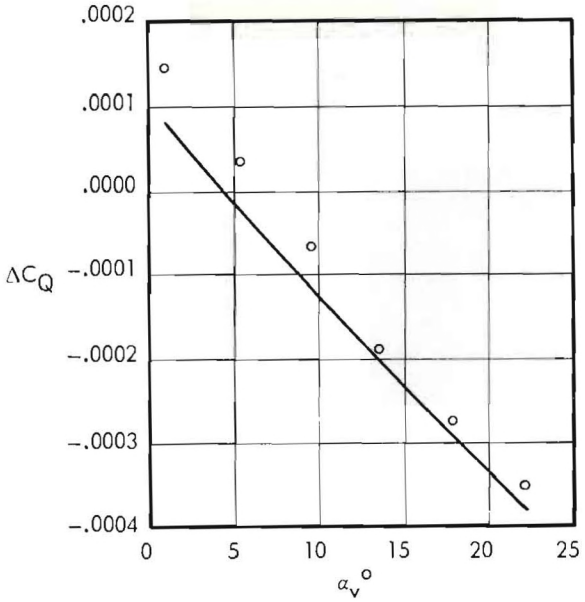

(h) V/ΩR = 0.26 (RPM = 1,000)

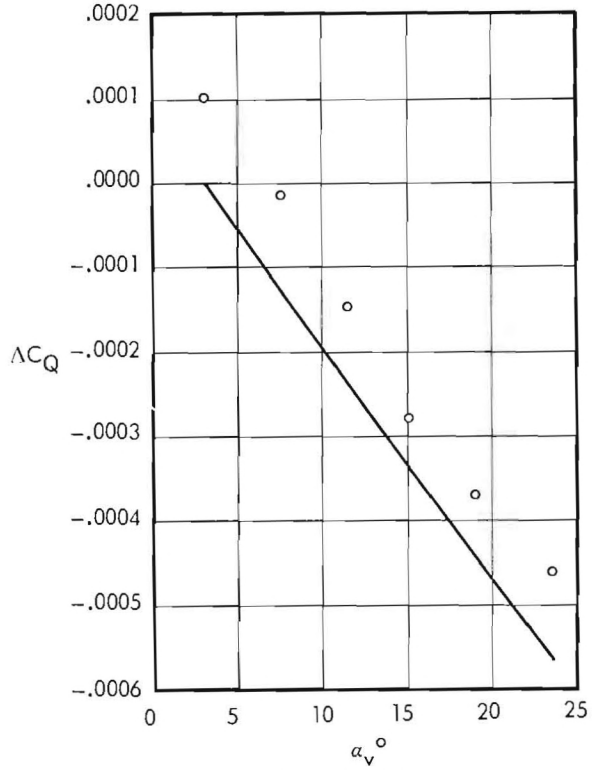

(i) V/ΩR = 0.32 (RPM = 800)

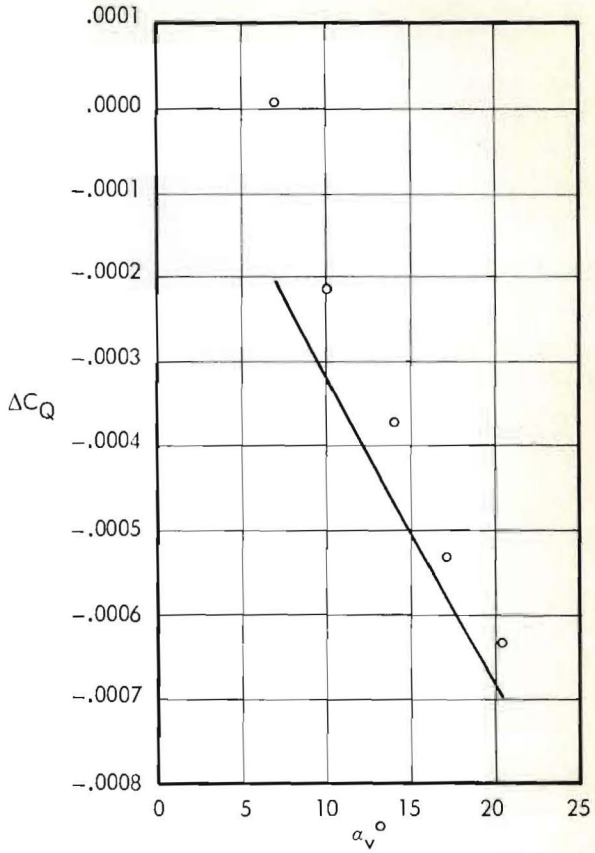

(j) V/ΩR = 0.43 (RPM = 600)

Figure 6 (Continued).

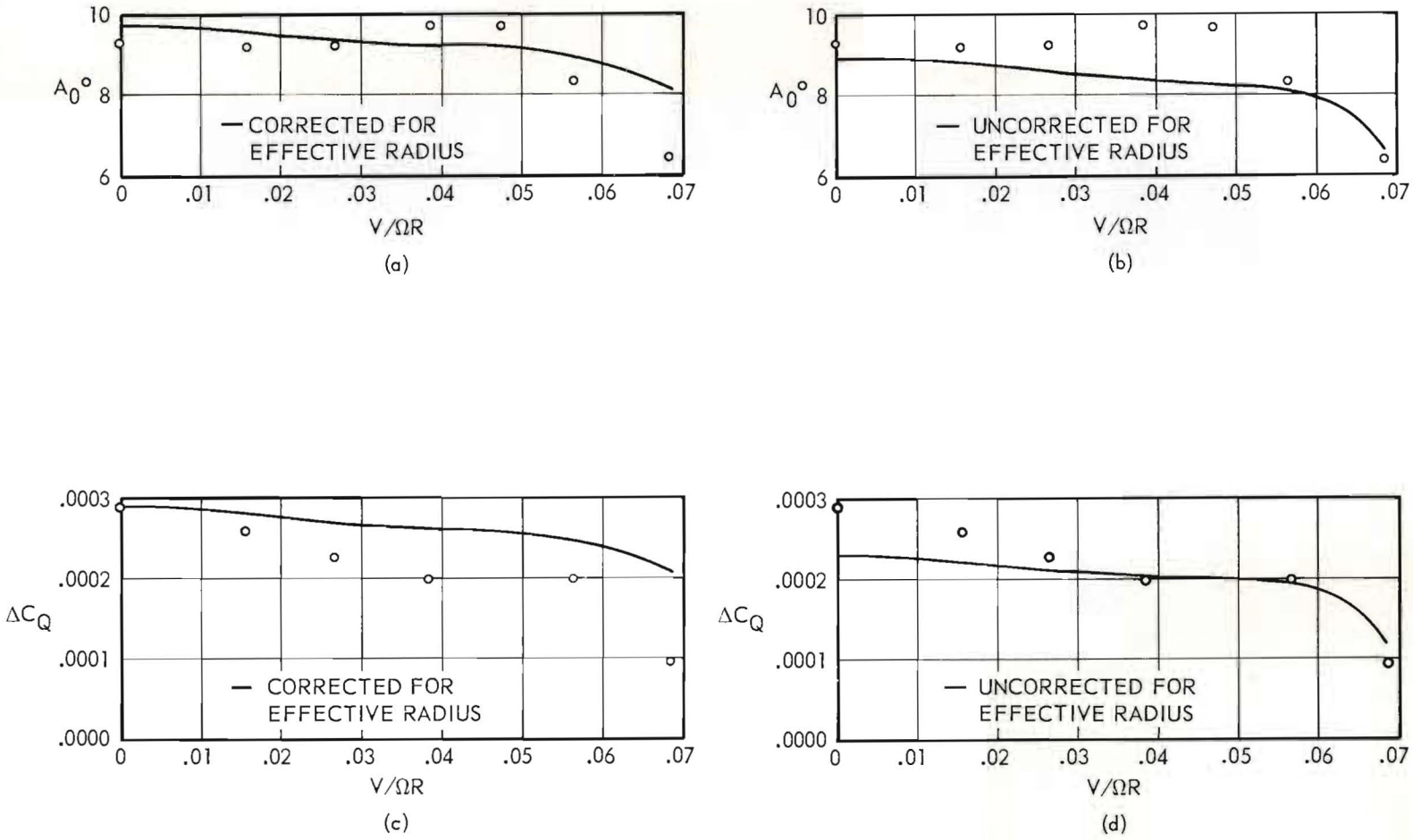

Figure 7. Experimental and Calculated Values of A_0 and ΔC_Q versus V/ΩR, (Vertical Descent, RPM = 1200).

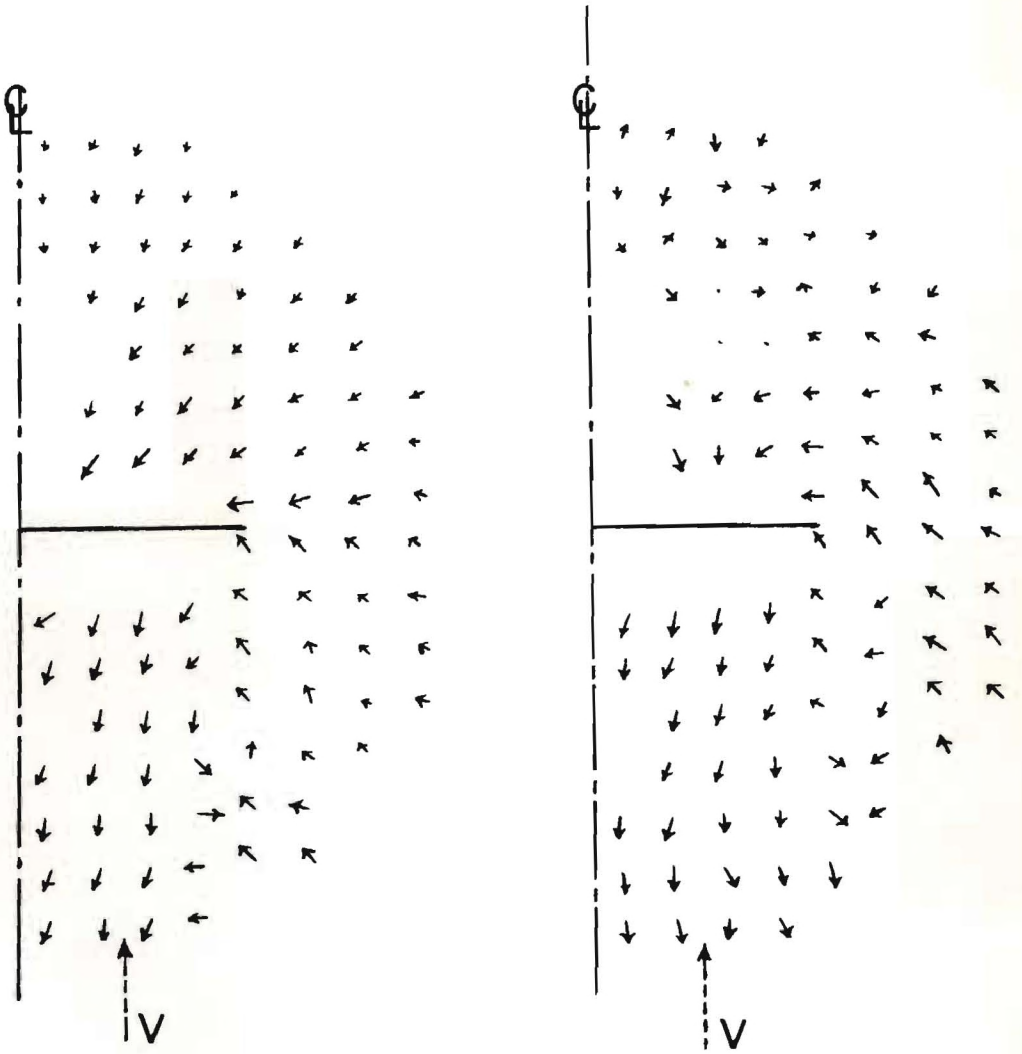

(a) C_T = .00398, $V/\Omega R$ = .0157, λ_z = .352

(b) C_T = .00398, $V/\Omega R$ = .0268, λ_z = .602

Figure 8. Vertical Descent Tuft Drawings.

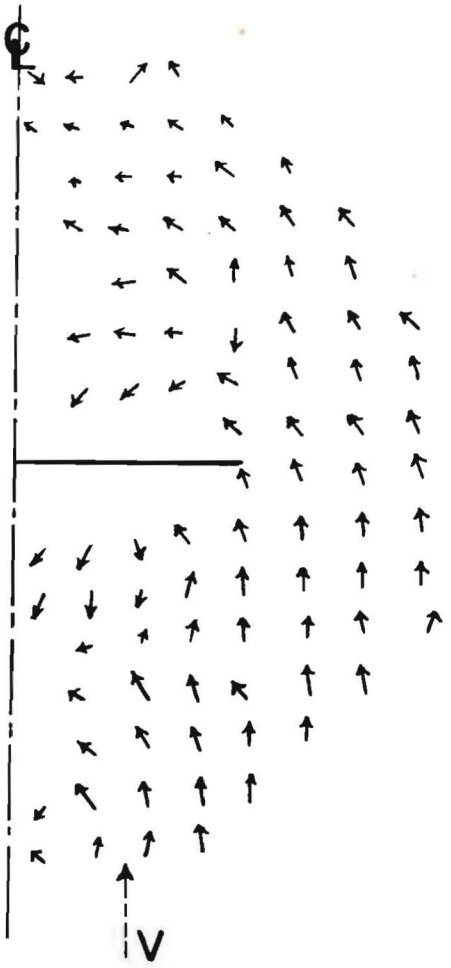

(c) $C_T = .00398$, $V/\Omega R = .0384$, $\lambda_z = .860$

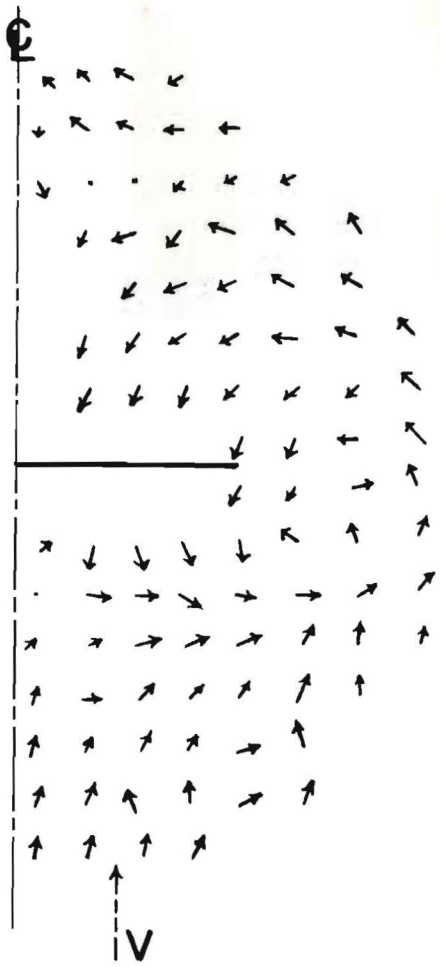

(d) $C_T = .00398$, $V/\Omega R = .0473$, $\lambda_z = 1.061$

Figure 8 (Continued).

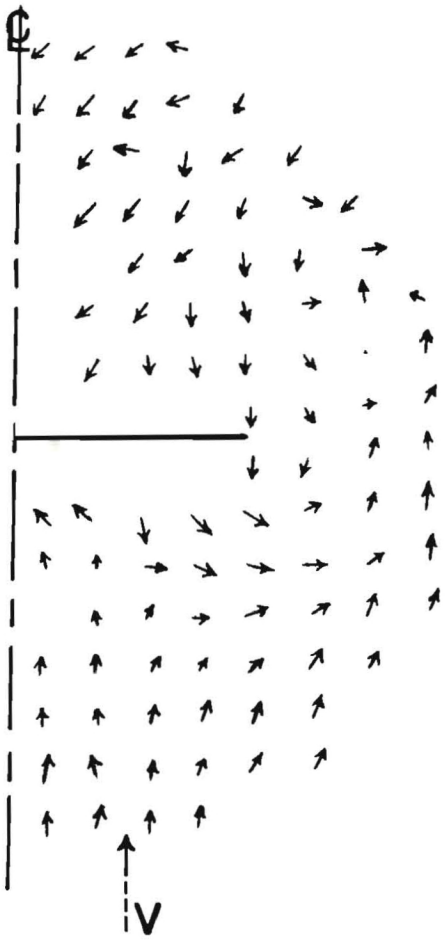

(e) C_T = .00398, $V/\Omega R$ = .0565, λ_z = 1.266

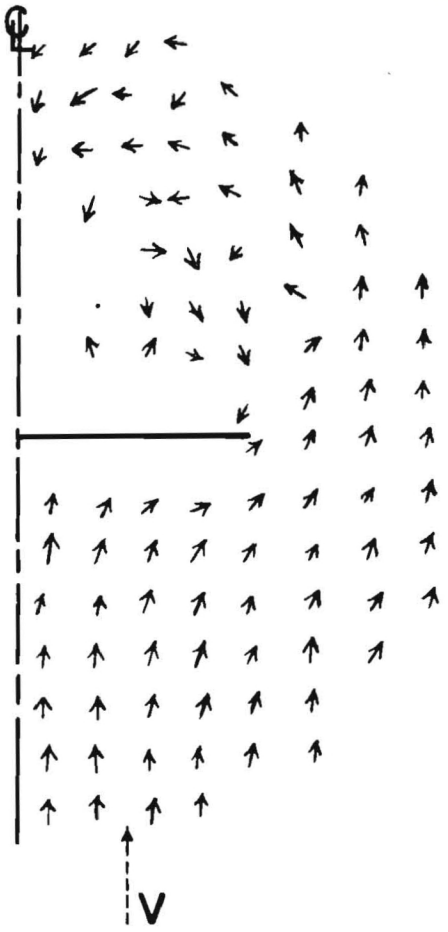

(f) C_T = .00398, $V/\Omega R$ = .0684, λ_z = 1.533

Figure 8 (Continued).

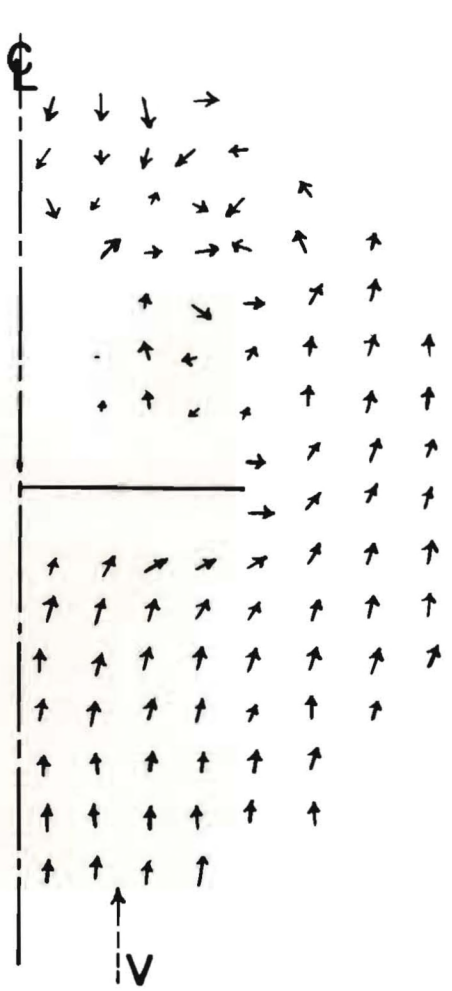

(g) C_T = .00398, $V/\Omega R$ = .0768, λ_z = 1.721

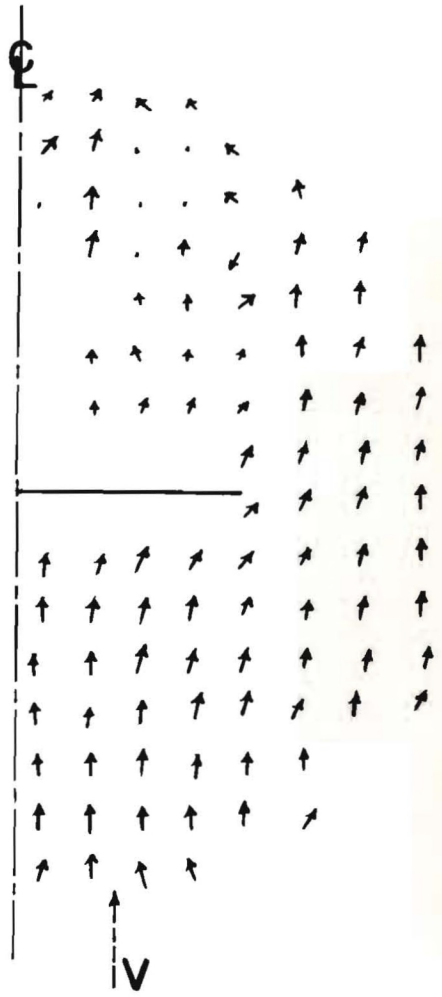

(h) C_T = .00398, $V/\Omega R$ = .0828, λ_z = 1.855

Figure 8 (Continued).

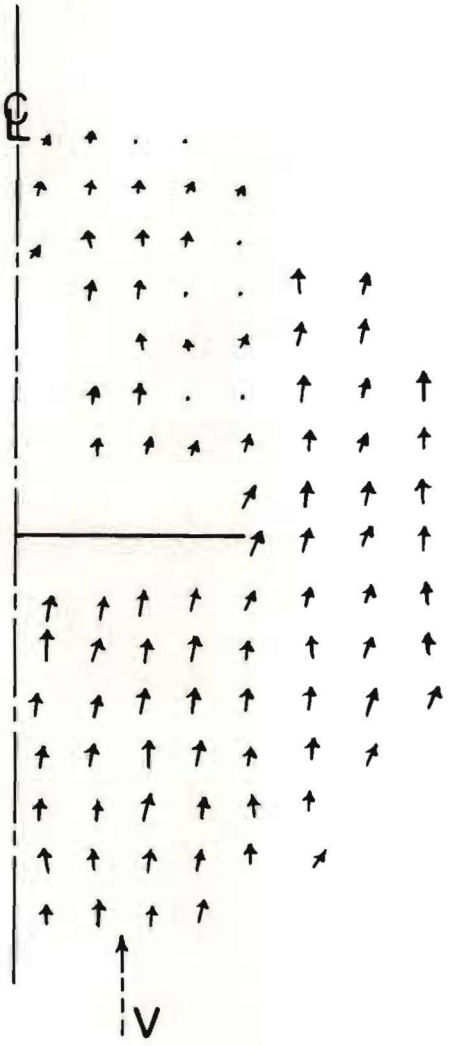

(i) C_T = .00398, $V/\Omega R$ = .0915, λ_z = 2.051

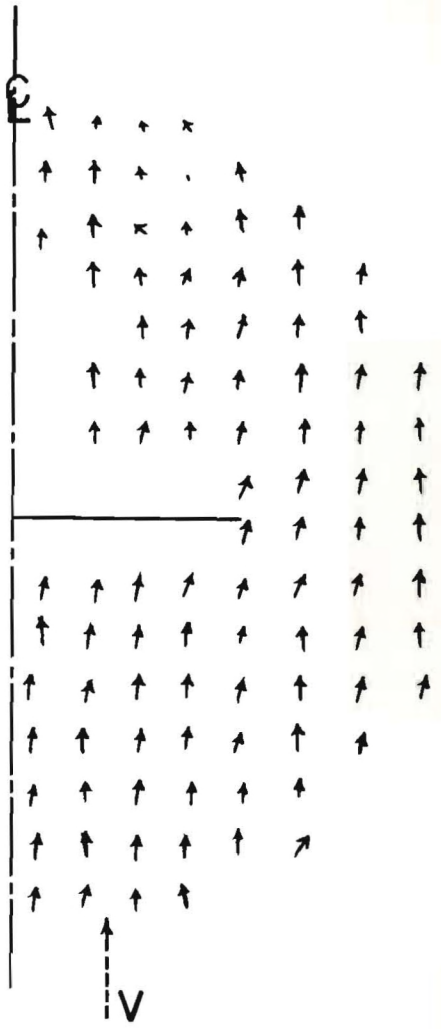

(j) C_T = .00398, $V/\Omega R$ = .0975, λ_z = 2.184

Figure 8 (Continued).

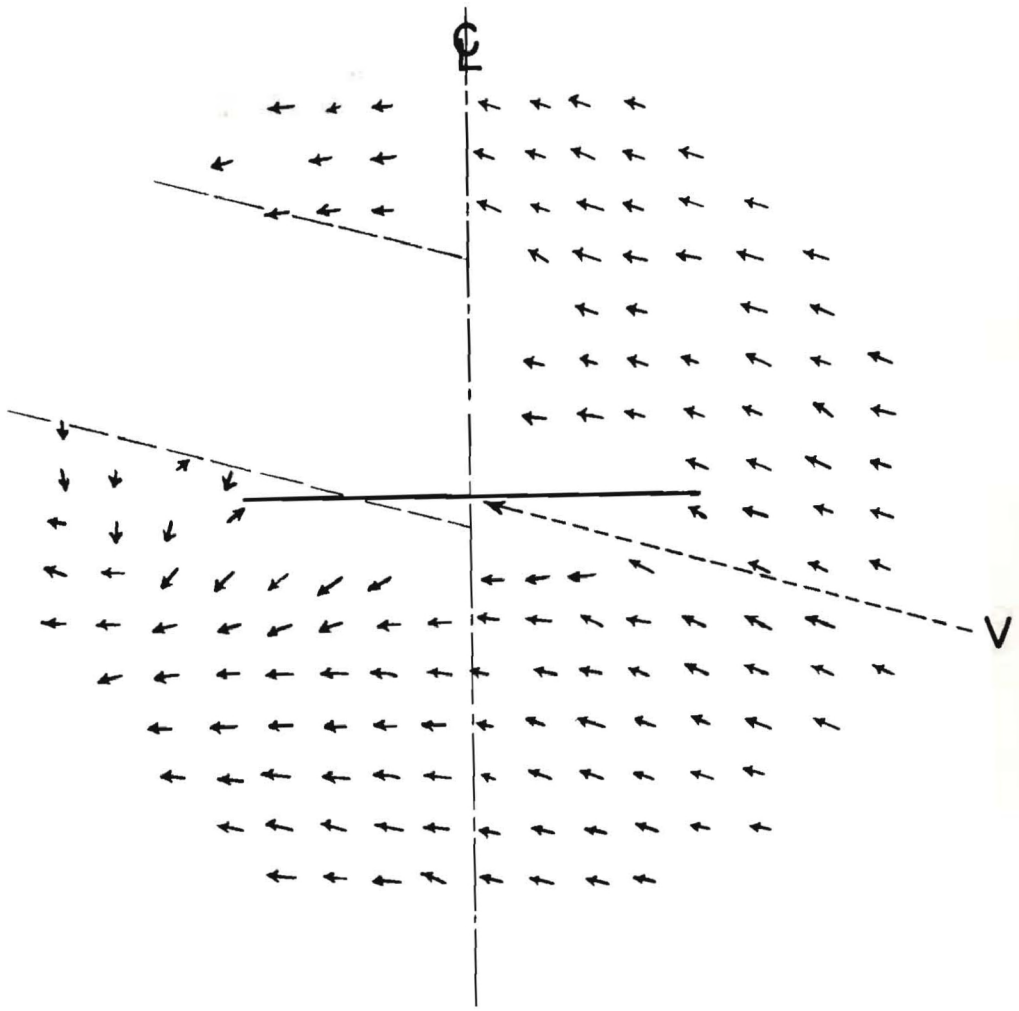

(a) $\alpha = 15°$, $C_T = .00404$,
$V/\Omega R = .0768$

Figure 9. Inclined Descent Tuft Drawings.

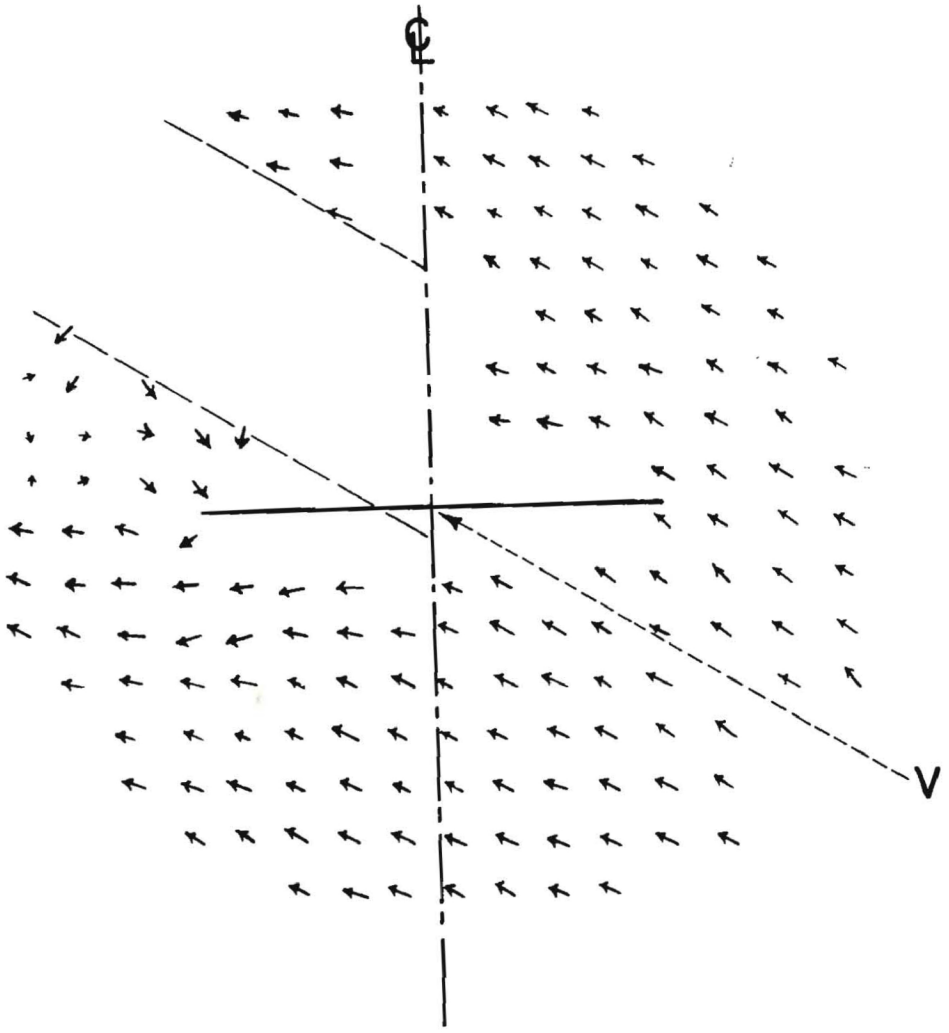

(b) $\alpha = 30°$, $C_T = .00404$,
$V/\Omega R = .0756$

Figure 9 (Continued).

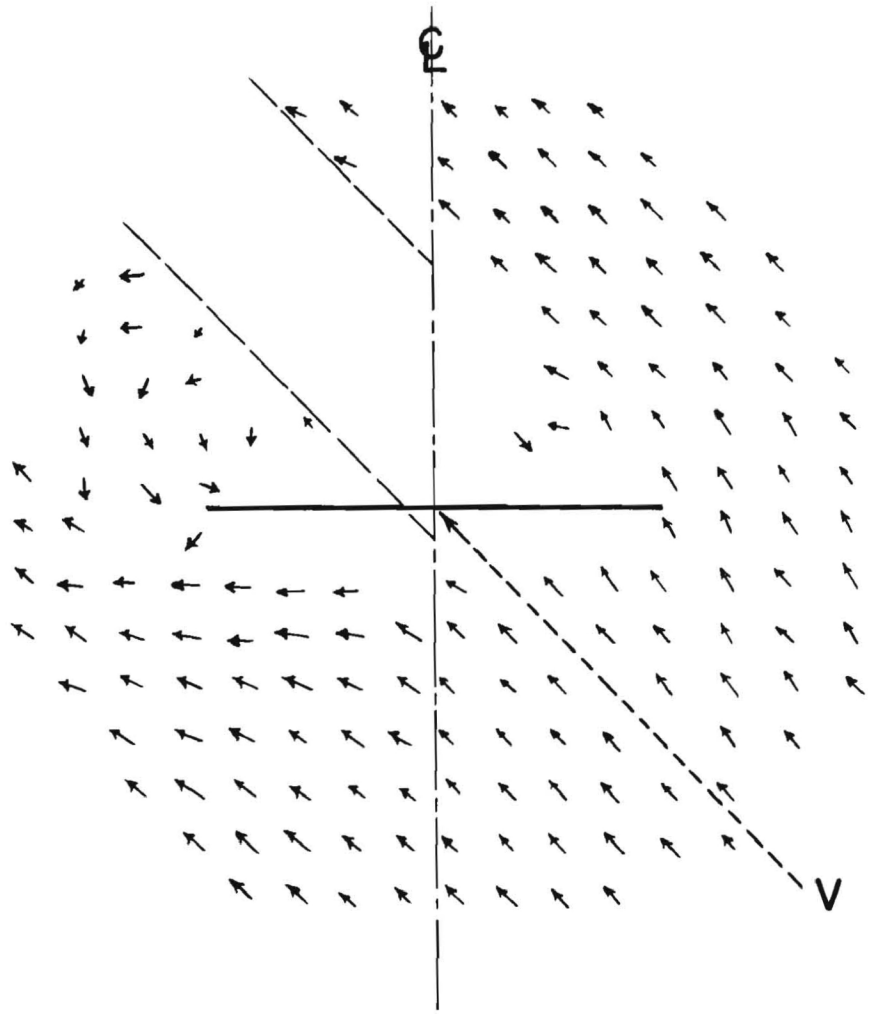

(c) $\alpha = 45^{\circ}$, $C_T = .00404$,
$V/\Omega R = .0756$

Figure 9 (Continued).

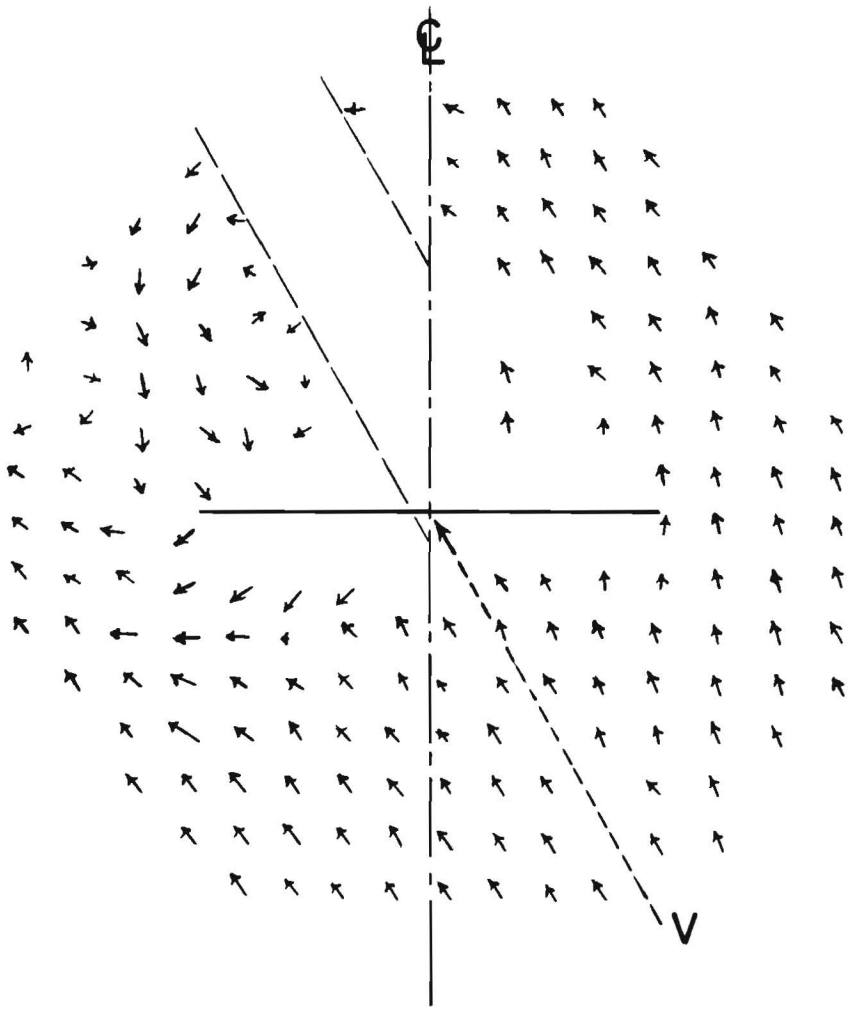

(d) $\alpha = 60°$, $C_T = .00404$,
$V/\Omega R = .0752$

Figure 9 (Continued)

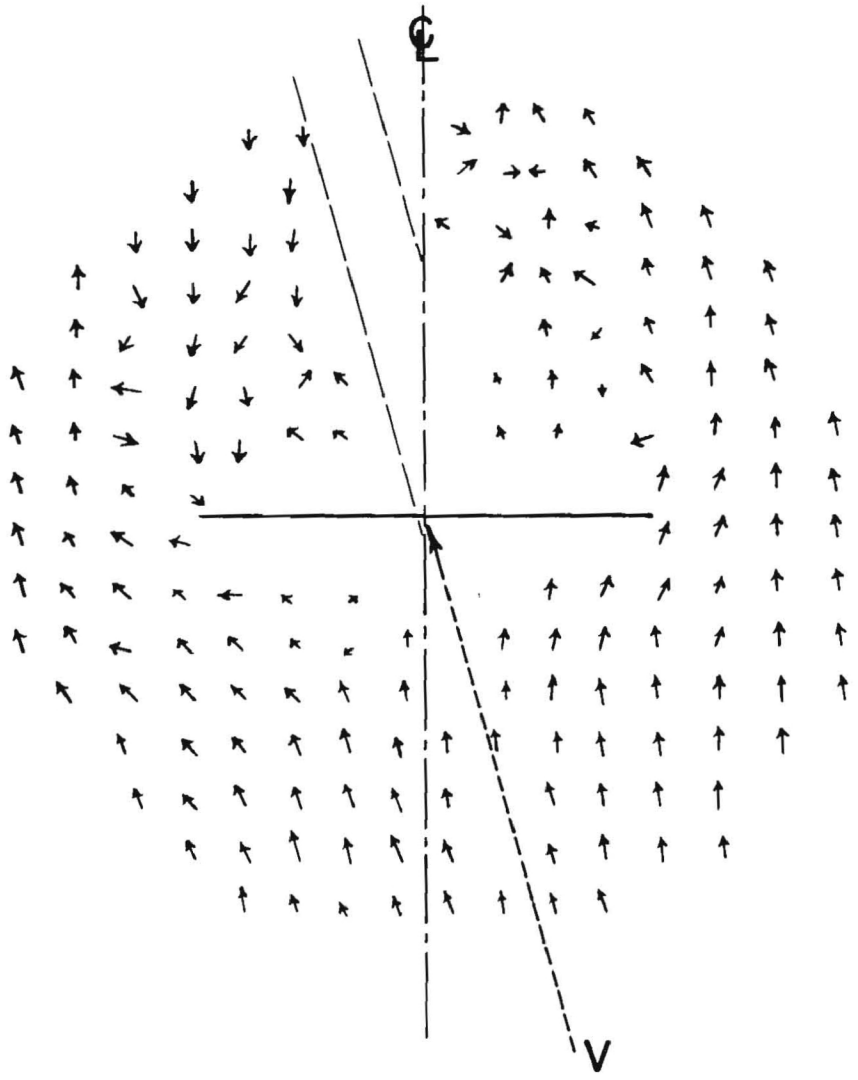

(e) $\alpha = 75°$, $C_T = .00404$,
$V/\Omega R = .0752$

Figure 9 (Continued).